Soft Matter

PAPER

View Article Online
View Journal

Cite this: DOI: 10.1039/d5sm00589b

Collision of surfactant-laden droplets: insights from molecular dynamics simulation†

Soheil Arbabi, *[ab] Piotr Deuar, [a] Rachid Bennacer, [c] Zhizhao Che [d] and Panagiotis E. Theodorakis [a]

We study the collision dynamics of surfactant-laden droplets and compare it with that of pure water droplets, with a focus on the bridge growth rate, energy balance, and disk dynamics, distinguishing the cases of head-on and off-centre collisions. By using molecular dynamics simulation of a coarse-grained model, it is found that initial linear scaling describes the first stage of the collision process, which is followed by power-law dynamics, in contrast to an initial thermal regime and a subsequent power-law behaviour observed for droplet coalescence. The transition between the two regimes occurs faster for surfactant-laden droplets. At higher collision velocities, the linear regime dominates the process with a gradual reduction of the power-law behaviour, reaching a situation in which the bridge growth is fully characterised by linear dynamics. The different behaviour of the droplets is presented in the form of a diagram of different scenarios, namely coalescence, separation, and splattering. In particular, it is found that higher velocities and larger offsets increase the likelihood of separation and splattering, with water droplets producing a greater number of satellite droplets due to reduced viscous damping. Also, a disk-like structure is observed as a result of collision, but it is less pronounced in the case of surfactant-laden droplets, due to higher dissipation of energy.

Received 8th June 2025,
Accepted 11th July 2025

DOI: 10.1039/d5sm00589b

rsc.li/soft-matter-journal

1 Introduction

Droplet collision and coalescence are ubiquitous phenomena in nature, which, for example, manifest in clouds and raindrops.[1] At the same time, these are relevant for applications in industry, such as liquid-fuel combustion and spray technology.[2] In view of the interest in these phenomena, various studies have been conducted towards obtaining a better understanding of them, but most of these investigations have thus far mainly focused on pure water or polymer droplets.[3–27] Although understanding collision and coalescence in the context of pure liquids is fundamental, most processes in industry (*e.g.* enhanced oil recovery[28]) as well as natural processes (*e.g.* formation of clouds[29]) take place in the presence of surfactants. Coalescence of such droplets has been previously explored by using molecular dynamics simulations of freely suspended[30,31] or sessile droplets,[32] since this method can provide a molecular-level resolution of the relevant processes, such as the surfactant mass transport mechanism. In this regard, a detailed description of the mass transport mechanism and bridge growth dynamics has been provided.[30–32] However, in various applications and phenomena, coalescence takes place while droplets move against each other with a relative velocity, in which case inertial effects are likely to play a more dominant role in the process, for example, by suppressing the initial thermal regime.[30,31] Currently, there is a lack of insight into the coalescence of colliding surfactant-laden droplets from a molecular perspective, which calls for further research in this area, especially in view of the interest in this process from a fundamental as well as an industrial perspective.

Several studies have overall provided valuable insights into the collision of droplets, especially for the case of pure liquids. In particular, Zhang *et al.*[33] conducted molecular dynamics simulations of head-on collisions of water droplets with a diameter of 10.9 nm for a wide range of Weber numbers, $We = \rho V^2 D_0/\gamma$, where ρ is the liquid density, V is the velocity of droplets, D_0 is the droplet diameter, and γ is the surface tension. This study has suggested that when the ratio of the expansion disk diameter to the droplet's initial diameter (D_d/D_0) is around 2.66, the liquid film becomes unstable, thus leading to rupture and eventually to the formation of cavities within the film. In this way, the initial kinetic energy of droplets is dissipated through viscous dissipation during the collision. Moreover, larger viscosity would lead to greater energy dissipation,

[a] Institute of Physics, Polish Academy of Sciences, Al. Lotników 32/46, 02-668 Warsaw, Poland. E-mail: arbabi@ifpan.edu.pl, arbabi@uwm.edu
[b] Department of Biomedical Engineering, University of Wisconsin-Milwaukee, Milwaukee, WI 53211, USA
[c] Université Paris-Saclay, CentraleSupélec, ENS Paris-Saclay, CNRS, LMPS - Laboratoire de Mécanique Paris-Saclay, Gif-sur-Yvette, 91190, France
[d] State Key Laboratory of Engines, Tianjin University, 300350 Tianjin, China

† Electronic supplementary information (ESI) available. See DOI: https://doi.org/10.1039/d5sm00589b

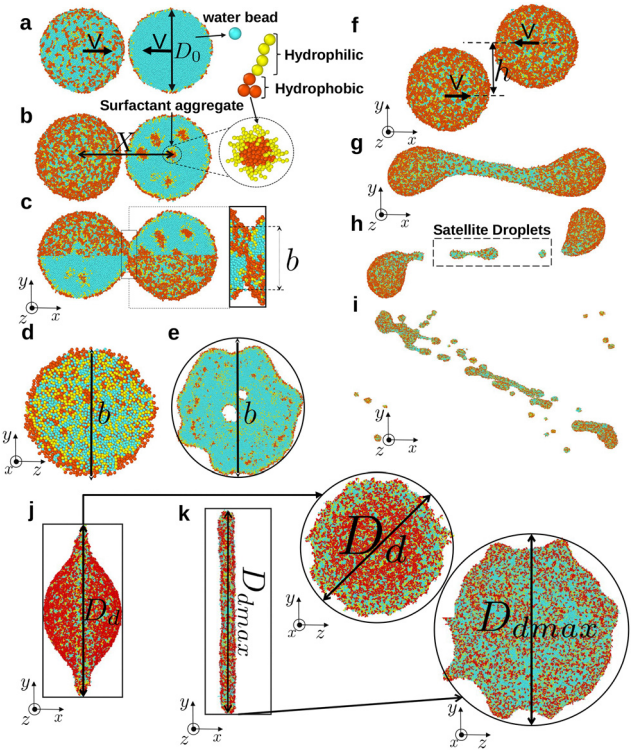

Fig. 1 Various stages of droplet collision for a number of scenarios differing in surfactant concentration and velocities. Scales are adjusted in the figure, so that the structural characteristics of the droplets and surfactant molecules are visible. The left column shows a head-on collision, while the right column shows an off-set one. Panels a and b show initial configurations before a head-on collision, below (a) and above (b) the critical aggregation concentration. In the latter case, a micelle and one of the participating surfactant molecules are shown. (c) A snapshot of an above CAC case early in the collision. The bridge diameter is indicated as b. (d) Snapshot of a disk that is formed as a result of a higher velocity collision, where the point of contact can keep expanding until the liquid forms a disk-like structure. This ultimately has a larger diameter (D_d, panel j) than the initial diameter of the droplets (D_0) in the direction perpendicular to the collision axis. At a high enough velocity (e), cavities (holes) may appear after reaching D_{dmax} (panel k), which is the maximum diameter that the disk reaches during the collision ($V = 2.2415\sigma/\tau$, $t = 152\tau$). (f) Configuration of the system before an offset collision with a vertical offset h. Various snapshots show different scenarios: (g) stretching after the collision (velocity $V = 1.3449\sigma/\tau$, $h = 0.5D_0$, $t = 150\tau$), (h) the formation of satellite droplets ($V = 1.3449\sigma/\tau$, $h = 0.5D_0$, $t = 290\tau$), and (i) splattering, which happens in the case of high-velocity collisions ($V = 2.9146\sigma/\tau$, $h = 0.3D_0$, $t = 140\tau$). (j) and (k) Bridge and disk formation during the head-on collision. When the bridge diameter equals the droplets' diameter ($b = D_0$), the disk between the droplets continues to grow if the kinetic energy (from the initial collision velocity) wins over the damping. For pure water and below CAC surfactant-laden droplets, this occurs when $V \simeq 0.67\sigma/\tau$, and $V \simeq 0.89\sigma/\tau$, respectively. We then denote the disk diameter as D_d, with side views provided under (j) and (k).

which could preserve the integrity of the expanding disk, that is to prevent the occurrence of cavities within it. Later, Liu *et al.*[34] identified various regimes based on the We number, including the splattering regime, and also suggested the 'periphery-sucking' mechanism to explain the thin middle and protruding edges of the expanding disk (*e.g.*, see Fig. 1e, j and k). Moreover, for high kinetic energy of the droplets, various scenarios are possible, namely, cavities in the bridge region, limited splattering, or the so-called divergent splattering (*e.g.* see Fig. 1i).

Molecular dynamics (MD) certainly offers specific advantages in investigating phenomena such as droplet collisions.[35–38] In particular, it allows for capturing the microscopic mechanisms, which also evolve very rapidly in time. However, MD studies have mostly been performed for systems without surfactants. For example, Tugend *et al.*[39] have carried out molecular dynamics simulations of large droplets (up to 2×10^7 molecules) for a range of Weber and Reynolds numbers. In their case, the coalescence, stable collision, holes, and shattering regimes have been observed, with the latter occurring after a critical We number and leading to the formation of satellite structures. Some of these regimes have also been observed previously by Greenspan and Heath.[40] The bouncing and coalescence regimes have also been investigated,[41,42] along with the effects of ambient pressure on nanodroplet collisions.[33,43] Also, Liu *et al.*[44] and Wang *et al.*[45] have investigated the coalescence of nanodroplets for a range of Weber and Ohnesorge numbers, observing coalescence, stretching separation, and shattering scenarios. Finally, oblique collisions of amorphous Lennard-Jones nanoparticles using molecular dynamics simulations as a function of collision velocity and impact parameter have been considered in the literature.[46]

Qian *et al.*[47] conducted an experimental investigation of the collision of binary droplets (water and hydrocarbon droplets) and constructed a phase diagram based on the observed collision behaviour as a function of offset and Weber number. Several distinct regimes were identified, namely (I) coalescence after minor deformation, (II) bouncing, (III) coalescence after substantial deformation, (IV) coalescence followed by separation for near head-on collisions, and (V) coalescence followed by separation for off-centre collisions. In particular, it has been found that regimes (II) and (III) do not exist in droplets solely consisting of water. Moreover, regimes IV and V lead to the formation of satellite droplets. Bouncing, which is due to a pressure build-up in the gap between the droplets, was not observed in the case of pure water droplets, which might be attributed to a higher surface tension and a lower viscosity in comparison with hydrocarbon droplets. Pan *et al.*[48] studied the bouncing and coalescence of surfactant-laden aqueous droplets by conducting experiments. Adding surfactants leads to a larger deformation of the surface, presumably, due to a lower surface tension, and a higher probability of bouncing. Experimental work by Krishnan *et al.*[3] on the collision classified five primary phenomenological outcomes, that is: slow coalescence (SC), bouncing (B), fast coalescence (FC), reflexive separation (RS), and stretching separation (SS).

The reflexive separation, which can be described as temporary coalescence followed by breakup into two main droplets, has also been observed by Huang *et al.*[49], and a larger number of satellite droplets is noted for higher We numbers. Munnannur *et al.*[50] have developed a model for predicting collision outcomes, satellite formation, and post-collision characteristics (velocity and droplet size) with predictions agreeing well with experimental results. Moreover, effects such as viscosity and surface tension have been discussed in a recent work by

Pan *et al.*[51] and predictions for a critical We number for satellite droplet formation have been made. In view of the role of viscosity and surface tension effects, which can be expressed by the Ohnesorge number, various similarities between droplet collisions and Plateau–Rayleigh instability could be drawn,[52,53] with a larger viscosity leading to less droplets in comparison with lower-viscosity scenarios.[54]

At this point, it is also worth mentioning a few fundamental quantities related to droplet coalescence before discussing our methods and results on droplets' collision. The rate at which the diameter of the bridge b (Fig. 1c) between droplets increases after their initial contact is crucial for understanding the dynamics of the coalescence process. In coalescence studies, this growth can generally be characterised by two primary fluid dynamics regimes: the viscous regime (VR) at early times and the inertial regime (IR) at later stages.[55,56] Additionally, recent MD simulations have identified a third regime, known as the thermal regime (TR),[6] which occurs during the very early stages of droplet coalescence when pinching takes place.[6,27,30–32]

In the viscous regime, the characteristic velocity, denoted as v_v, can be expressed as γ/η, where γ is the surface tension and η is the viscosity. Moreover, the Reynolds number can be expressed as $\mathrm{Re} = \rho V b/\eta$, where V is the velocity and b is the bridge diameter (Fig. 1c), which in the viscous regime becomes $\rho\gamma b/\eta^2$. Since the bridge length is very small in this regime, viscous forces dominate regardless of the values of γ and η, leading to $\mathrm{Re} \ll 1$. As coalescence progresses into the inertial regime (IR), the bridge velocity scales as $V_i \sim \sqrt[4]{\gamma/\rho}$. The crossover between the viscous and inertial regimes is expected to occur when $\mathrm{Re} \sim 1$. The characteristic viscous time scale of $t_v = \eta R_0/\gamma$ and the characteristic inertial time scale of $t_i = \sqrt{\rho R_0^3/\gamma}$ have been suggested by a lattice Boltzmann study,[57] where $R_0 = D_0/2$ (Fig. 1a).

In the VR, where intermolecular forces predominantly drive the coalescence process, the bridge diameter for the coalescence of freely suspended droplets has been proposed to scale linearly with time, expressed as $b \propto t$, with some suggesting logarithmic corrections, that is $b \propto t \ln t$.[7,58] For the IR, power-law scaling has been proposed for the bridge diameter, specifically $b \propto \sqrt{t}$.[7,58] Experimental studies on the coalescence of water droplets support this scaling behaviour.[7–9,57,59] In addition, it has been suggested that the inertia of the droplets cannot be ignored during the initial stage of coalescence. This initial stage is then better described as an inertially limited viscous (ILV) regime, where a linear scaling of the bridge dimension with time has been proposed.[56,60] However, the existence of the ILV regime seems to remain questionable with Eggers *et al.* arguing that the bridge region remains purely viscous.[61]

All-atom molecular dynamics simulations of two-dimensional (cylindrical) pure water droplets have revealed multiple liquid bridges forming on the droplet surfaces and connecting them, which are highly affected by thermal fluctuations at the molecular level and indicate the so-called thermal regime at the beginning of the coalescence process.[6] In this case, once the bridge length exceeds a thermal length scale, estimated as $l_T \approx (k_B T/\gamma)^{1/4} {R_0}^{1/2}$, the system transitions to a hydrodynamic regime. Here, γ is the surface tension, T is the temperature, and k_B is the Boltzmann constant. We have previously demonstrated the presence of the thermal regime followed by the inertial regime for both freely suspended[30,31] and sessile droplets[32], including both the case of pure water droplets as well as that with surfactant-laden droplets. A summary of bridge growth scalings in the case of zero-velocity droplet-coalescence found in our earlier studies based on the same MD model are reported in Table 1.

Table 1 Summary of bridge growth scaling within the inertial regime in freely suspended and sessile droplets from MD studies based on the same model.[27,30–32]

System	Bridge dimension growth (b)
Suspended water and surfactant-laden droplets[30,31]	$b \sim t^{0.5–0.6}$
Sessile water and surfactant-laden droplets ($\theta_s \geq 90^\circ$)[32]	$b \sim t^{0.5–0.6}$
Sessile water and surfactant-laden droplets ($\theta_s < 90^\circ$)[32]	$b \sim t^{0.6–0.8}$
Sessile polymer droplets ($\theta_s > 90^\circ$)[27]	$b \sim t^{0.28–0.38}$
Sessile polymer droplets ($\theta_s < 90^\circ$)[27]	$b \sim t^{0.29–0.45}$

Despite progress in the study of droplet collision, especially from the point of view of molecular dynamics simulations of large systems,[39] which is suitable for describing the microscopic details of this fast process, the role of surfactants has largely remained unexplored. To fill this gap, this study builds on previous work on the coalescence of pure and surfactant-laden water droplets[30,31] and explores the head-on and off-centre collision for water and surfactant-laden droplets by means of molecular dynamics (MD) simulation based on a coarse-grained force-field. Our findings suggest that the presence of surfactants significantly affects the dynamics of collisions and, in particular, the head-on collisions, with significant differences appearing in comparison with the droplet coalescence at zero velocity.[30,31]

The paper is organised as follows: in the following section, we detail our model and methodology, while in Section 3, we present the analysis and classification of the results of head-on and off-centre collisions with details provided on the oscillation states and final states of the droplets. Finally, Section 4 offers conclusions drawn from this study.

2 Model and methods

Before providing more technical detail on the simulations, we first give a brief overview of the different scenarios observed during our simulations. Droplets can collide head-on or off-centre (Fig. 1). A head-on or nearly head-on (paraxial, small offset, h) collision leads to the creation of a disk with diameter D_d as it goes through the bridge formation stage and coalescence, as shown in Fig. 1j and k. In this case, D_d is greater than the diameter D_0 of the initial droplet. This disk expands (Fig. 1d, j and k), and, moreover, holes (cavities) will form

within the disk (Fig. 1e), which might be attributed to the fact that the kinetic energy during the disk expansion wins over the viscous dissipation. In Fig. 1c, the bridge, and, in Fig. 1j and k, the disk are depicted to better highlight their differences. In the case of off-centre collisions (Fig. 1f–i), significant stretching of the liquid (Fig. 1g) and the creation of satellite droplets are observed (Fig. 1h). In addition, at higher collision velocities, both the head-on and off-centre droplets' collision can lead to splattering (Fig. 1i).

At a more technical level, we conduct our research using MD simulations based on the SAFT (Statistical Associating Fluid Theory) γ-Mie force-field.[62–67] In the case of surfactant-laden droplets, the SAFT-γ Mie theory force-field[68] has been accurate in reproducing key properties of water–surfactant systems, such as phase behaviour, contact angles of droplets, and surface tension.[69–73] Moreover, as a coarse-grained (CG) force-field, it enables the simulation of relatively large droplets, which in turn allows for a careful examination of surfactant-related mechanisms and relevant properties as has been done in the case of the coalescence of surfactant-laden droplets.[30–32] Other applications of droplet-related phenomena with this force-field included the study of the superspreading of surfactant-laden droplets.[69,70,74–76]

In the SAFT γ-Mie force-field, interactions between different coarse-grained (CG) beads within a distance smaller than r_c are described *via* the Mie potential

$$U(r_{ij}) = C\varepsilon_{ij}\left[\left(\frac{\sigma_{ij}}{r_{ij}}\right)^{\lambda_{ij}^{r}} - \left(\frac{\sigma_{ij}}{r_{ij}}\right)^{\lambda_{ij}^{a}}\right], \quad r_{ij} \le r_c, \tag{1}$$

where

$$C = \left(\frac{\lambda_{ij}^{r}}{\lambda_{ij}^{r} - \lambda_{ij}^{a}}\right)\left(\frac{\lambda_{ij}^{r}}{\lambda_{ij}^{a}}\right)^{\frac{\lambda_{ij}^{a}}{\lambda_{ij}^{r} - \lambda_{ij}^{a}}}. \tag{2}$$

i and j are the bead types, σ_{ij} indicates the effective bead size, and ε_{ij} is the interaction strength between any beads of type i and j. $\lambda_{ij}^{a} = 6$ and λ_{ij}^{r} are Mie potential parameters, while r_{ij} is the distance between two CG beads. The chosen units are for the length, σ, energy, ε, mass, m, and time τ corresponding to real units as follows: $\sigma = 0.43635$ nm, $\varepsilon/k_B = 492$ K, $m = 44.0521$ amu and $\tau = \sigma(m/\varepsilon)^{0.5} = 1.4062$ ps. The simulations were performed at room temperature ($T = 25$ °C), which corresponds to $T = 0.6057\varepsilon/k_B$ in simulation units. A universal cutoff $r_c = 4.583\ \sigma$ was applied to all nonbonded (Mie) interactions.

A surfactant of type CiEj (Fig. 2b) is considered in this study, *i.e.* C10E4. In general, in the case of CiEj surfactants, a hydrophobic alkane CG 'C' bead represents a $-CH_2-CH_2-CH_2-$ group of atoms, while a hydrophilic CG 'EO' bead represents an oxyethylene group $-CH_2-O-CH_2$. A water CG 'W' bead corresponds to two water molecules (Fig. 2a). The non-bonded interaction parameters between the above chemical groups are reported in Table 2, while the mass of each CG bead is documented in Table 3.

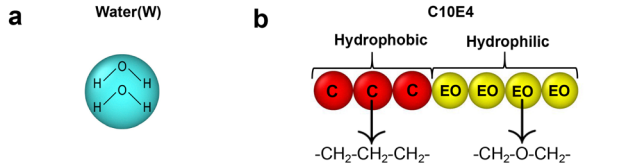

Fig. 2 Coarse-grained representation of two water molecules (a) and a surfactant molecule (b). The hydrophobic beads of the surfactant are shown in red, while the hydrophilic ones are in yellow.

Table 2 Summary of Mie interaction parameters (eqn (1)). $\lambda_{ij}^{a} = 6$

i–j	σ_{ij} [σ]	ε_{ij} [ε/k_B]	λ_{ij}^{r}
W–W	0.8584	0.8129	8.00
W–C	0.9292	0.5081	10.75
W–EO	0.8946	0.9756	11.94
C–C	1.0000	0.7000	15.00
C–EO	0.9653	0.7154	16.86
EO–EO	0.9307	0.8067	19.00

In the case of surfactant chains, a bond potential is required to tether consequent beads along the chain, which in the case of this model is

$$V_{bond}(r_{ij}) = 0.5k(r_{ij} - \sigma_{ij})^2, \tag{3}$$

where the harmonic constant is $k = 295.33\varepsilon/\sigma^2$. Moreover, EO beads experience a harmonic angle potential,

$$V_\theta(\theta_{ijk}) = 0.5k_\theta(\theta_{ijk} - \theta_0)^2, \tag{4}$$

where θ_{ijk} is the angle formed by three consecutive beads i, j, and k, (regardless of bead type), $k_\theta = 4.32\varepsilon/\text{rad}^2$, and $\theta_0 = 2.75$ rad is the equilibrium angle. Additional details about the model can be found in previous studies.[69,74,76]

To prepare the initial configuration for each system, as done in earlier studies,[30,31] individual droplets were first equilibrated within the NVT ensemble using the Nosé–Hoover thermostat through the LAMMPS package[77] with an integration time step of $\delta t = 0.005\tau$. Each initial droplet contained 10^5 beads in the simulations, with approximately 5% evaporating into the gas phase. The droplet diameters were $\sim 53\sigma$ (approximately 23 nm), consistent with several previous studies.[6,30,31] Additional information and the database required to reproduce the data are provided in the ESI,† section titled Simulation Parameters and Data Availability. Attention was given not only to monitoring the system's energy but also to ensuring that the surfactant clusters reached dynamic equilibrium, allowing each cluster to diffuse a distance many times its size. Once the individual droplets were equilibrated, the two droplets, along with the surrounding gas, were positioned next to each other as depicted in Fig. 1a in the case of a head-on collision or with the desired offset, h (Fig. 1f), in the case of off-centre collisions, preserving in the two-droplet system the same number of particles per volume as in the single-droplet simulations. At this stage, the desired offset (h) and centre-of-mass velocities (V) are assigned to each droplet, and the collision simulation is performed in the NVE ensemble with a time step of $\delta t = 0.001\tau$. The smaller time step here ensures that the MD simulations

Table 3 Mass of the CG beads

Bead type	Mass [m]
W	0.8179
C	0.9552
EO	1.0000

remain stable during the integration of the equations of motion for the particles for the highest We numbers of this study.

The final size of the simulation box was selected to be sufficiently large to prevent any interactions between mirror images of the droplets due to the presence of periodic boundary conditions in all directions, and moreover, to ensure that the box is large enough to be able to observe the elongated structures in the offset collisions as shown in Fig. 1g and h. We simulate surfactant-laden droplets below and above the critical aggregation concentration (CAC) as well as pure water droplets for comparison. Fig. 1a illustrates a typical initial snapshot for cases below CAC, while Fig. 1b shows a case above CAC. A summary of the mean values of various properties for our systems with surfactants is given in Table 4. Information on systems that have been studied in the literature (*e.g.* We numbers, drop-size ratios and sizes, ambient medium, *etc.*) can be found in ref. 50, while the range of parameters considered in recent molecular dynamics simulations and the span of We numbers for which bouncing, coalescence, stable collision, holes, and shattering occur can be found in ref. 39. Finally, we calculated the surface tension of the water droplet to be approximately 72 mN m^{-1}, while that of the surfactant-laden droplets discussed above CAC is approximately 29 mN m^{-1}. Considering these surface tension values, the Weber numbers for water droplets in this system range from near 0, corresponding to coalescence, up to approximately 184, this upper limit occurs at a velocity of $V \simeq 2.4662\sigma/\tau$. For surfactant-laden droplets, the Weber numbers can be even higher due to the reduced surface tension, which enhances the influence of inertial forces relative to surface tension. To examine comparable, matching cases for both pure water droplets and droplets laden with surfactants, we chose here to present our results based on the velocity, instead of dimensionless numbers. Moreover, determining exact values for the viscosity of complex systems (*e.g.* those containing surfactants) in molecular dynamics simulations with potentials of hard-core interactions can be challenging. For this reason, a discussion of the results in the context of Reynolds numbers, as is done in other studies,[39] is omitted here.

Table 4 Properties of individual droplets (equilibrium)

Concentration (wt%)	Diameter (σ)	Water beads[a]	Surfactant molecules
Water			
—	52.5	95 882	—
C10E4			
6.25	53.1	90466.1	714
35.48	54.1	65746.7	4286
CAC ≈ 7.5 wt%			

[a] Indicates the average number of water beads.

3 Results and discussion

3.1 Head-on collision

The first part of this study focuses on head-on collisions, where two droplets collide face-to-face with zero offset (Fig. 1a and b). Considering that the gravitational potential energy and the dissipation away from the bridge are not relevant (the droplet size is smaller than the capillary length of water, for example, see Table 4 for the droplet sizes in this study), the approximate energy balance of the relevant elements of the system can be expressed as follows:

$$E_{k1} + E_{s1} = E_{k2} + E_{s2} + W. \quad (5)$$

Here, E_{k1} and E_{k2} are the kinetic energy of each droplet and E_{s1} and E_{s2} are the surface energies of each droplet that can be estimated as follows:[33,78]

$$E_{s1} = 2\pi {D_0}^2 \gamma, \quad (6)$$

$$E_{k1} = \frac{\pi {D_0}^3 \rho V^2}{6}, \quad (7)$$

where D_0 is the diameter of the droplets. The quantity W is the viscous dissipation from the initial state to a maximum spreading state which is defined as follows:[33,78]

$$W = 2\int_0^{t_c} \mathrm{d}t \int_\Omega \mu V {D_0}^2 (\beta^5 - 1) = \frac{3\pi}{80} \mu V {D_0}^2 (\beta^5 - 1), \quad (8)$$

where β is the maximum spreading factor

$$\beta = \frac{D_{\mathrm{dmax}}}{D_0}. \quad (9)$$

Here, D_{dmax} is the maximum spreading diameter, which is the diameter of the disk in our case. Moreover, Zhang *et al.*[33] obtained the following relation between the maximum spreading factor, Re number, and We number:

$$\frac{3}{80}(\beta^5 - 1) + \frac{\mathrm{Re}}{\mathrm{We}}\left(\beta^2 + \frac{1}{3\beta} - 2\right) - \frac{\mathrm{Re}}{6} = 0 \quad (10)$$

Fig. 3 shows the evolution of the spreading factor, β, during the collision of water droplets and surfactant-laden droplets. Pure water droplets and droplets with surfactant concentration below CAC have a very similar trend, while above CAC (CAC ≈ 7.5 wt%), β obtains lower values at similar collision velocities. Moreover, the maximum ratio for which cavities appear, β = 3.0 ± 0.2, as estimated from this study, is reasonably close to the value of 2.66 reported in ref. 33, though slightly higher.

3.1.1 Bridge dynamics. During the first part of the collision, a bridge of diameter $b < D_0$ is formed between the two droplets (Fig. 1c). In our previous studies[30,31] related to the coalescence of freely suspended droplets, we have demonstrated that the bridge initially appears as a small overlap with fluctuating diameter b within the thermal regime, followed by the power-law growth of the diameter in the inertial regime. In the case of droplet collisions, we observe the emergence of a

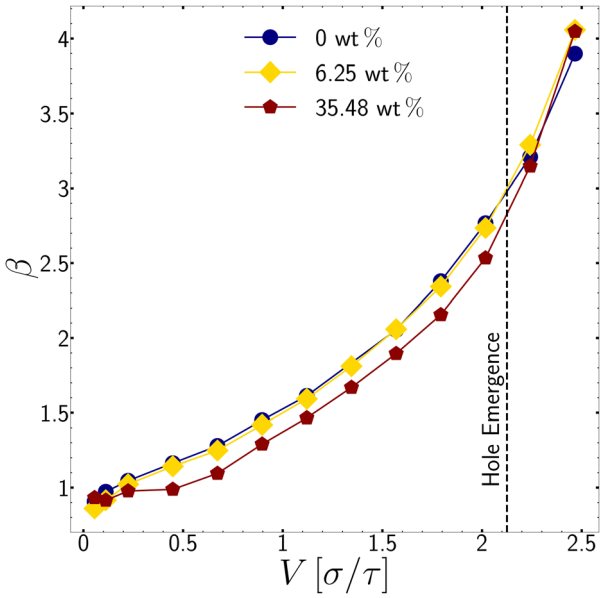

Fig. 3 Comparison of $\beta = D_{dmax}/D_0$ parameter that quantifies the relative size of the disk for different collision velocities during head-on collisions. In all cases, when the velocity was $V \simeq 2.24\sigma/\tau$, cavities were observed in the bridge.

linear regime. This linear regime is more pronounced in the collision process for larger velocities, when the collision time becomes smaller.

Fig. 4 presents the dynamics of the bridge diameter in the case of pure water (Fig. 4a) and surfactant-laden (Fig. 4b) droplets (above CAC), respectively. In each panel, the linear regime is fitted by red dashed lines with slopes m_v reported in Tables S1 and S2 of the ESI,† for Fig. 4a and b, respectively. The inertial regime is fitted *via* a black dashed line and the power-law exponents are reported as α_i in the same tables.

At medium velocities of droplet collision (from $0.056\sigma/\tau$ to $0.2242\sigma/\tau$ for water and from $0.056\sigma/\tau$ to $0.4483\sigma/\tau$ for surfactant-laden droplets above CAC in our data), two regimes exist. Both the linear and power-law growth of bridge size are steeper in the case of pure water droplets. At higher velocities (above $0.2242\sigma/\tau$ for water and above $0.4486\sigma/\tau$ for surfactant-laden droplets in our data), the power-law regime disappears. Here, the kinetic energy is large and the impact energy cannot be completely damped by viscous dissipation and surface energy. For this reason, the power law growth characteristic of slow coalescence does not appear. Surfactant-laden droplets have higher viscosity and smaller β (Fig. 3) than water droplets, which implies higher rates of viscous dissipation of energy that lead to smaller expansion of the bridge between the droplets. It can be observed that surfactant-laden droplets were able to maintain coalescence behaviour up to higher velocities, where $V \simeq 0.4483\sigma/\tau$, while water droplets can sustain the coalescence regime only up to $V \simeq 0.2242\sigma/\tau$. It is worth mentioning that, in the case of surfactant-laden droplets (Fig. 4b), the values of b for the coalescence case ($V = 0\sigma/\tau$) initially increase more slowly compared to the other data sets. However, there is a crossing with the collision cases at velocities between $0.056\sigma/\tau$ and

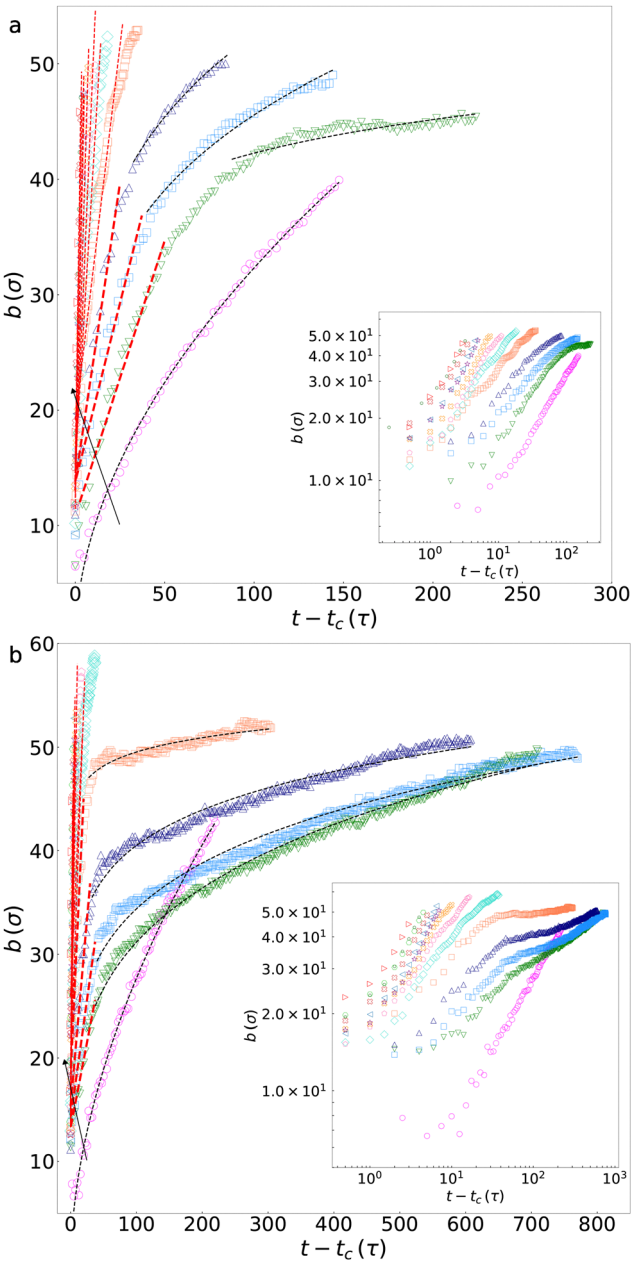

Fig. 4 Bridge dynamics during head-on collisions of (a) water and (b) surfactant-laden (above CAC) droplets at different velocities. In each case, the linear fit is represented by a red dashed line with the fitting parameter m_v, while the power-law fit is illustrated by a black dashed line with the fitting parameter α_i. The black arrow indicates the progression from lower to higher velocities in the range 0 to $2.4662\sigma/\tau$, and the details of the fitting parameters are provided in Tables S1 and S2 of the ESI.† In the plots, t_c indicates that all measurements are taken from the time (t_c) droplets make contact.

$0.1121\sigma/\tau$, indicating that the bridge growth after coalescence can eventually turn out faster than after a collision. This phenomenon might be explained by the fact that when droplets are more viscous, the kinetic energy during low-velocity collisions is significantly dampened. As a result, the energy becomes insufficient to continue the bridge growth, and the effect ends up actually delaying it.

3.1.2 Disk dynamics. We further analyse the disk diameter during the collision process (Fig. 1d, e, j and k). In the previous section, we considered the bridge up to the moment when its diameter b exceeds the initial droplet diameter D_0. However, in a fast enough collision, the point of contact can keep expanding until the liquid forms a disk-like structure that has a larger diameter than the initial droplets, but usually a shorter thickness in the collision direction than D_0 (the droplet's initial diameter is around 50σ). This disk can expand until the viscous dissipation consumes the initial kinetic energy of the expanding disk.

The average disk diameter (D_d in Fig. 1j) is plotted over time for water droplet collisions (Fig. 5a) and surfactant-laden droplet collisions above CAC (Fig. 5b). The most visible difference between these cases is that for water droplets at high velocities (runs with V above $1.5691\sigma/\tau$), the disk diameter starts to oscillate after reaching its maximum diameter. In contrast, for surfactant-laden droplets (above CAC), there is no fluctuation; instead, the disk shrinks monotonically after reaching its maximum diameter. The absence of fluctuations in the case of surfactant-laden droplets may be due to the greater viscous dissipation, which more efficiently absorbs the initial kinetic energy.

In all cases, we observed the appearance of vacuum holes (cavities) during the runs at velocities around $2.2415\sigma/\tau$. In Fig. 6, the disk is depicted for pure water (Fig. 6a–d) and surfactant-laden droplets above the CAC (Fig. 6e–h), at a velocity of $V = 2.2415\sigma/\tau$. The plot illustrates the thickness of the disk and the geometry of the holes. It demonstrates that in the case of pure water, there is a stronger flow towards the rim of the disk, leading to a thinner middle region and larger holes. Conversely, in the case of surfactant-laden droplets, there is weaker flow, resulting in a thicker middle region and smaller holes. The high kinetic energy of the expanding disk leads to the thinning of the middle region of the disk and the formation of holes. Moreover, in water droplets and droplets below the CAC, lower viscosity results in less damping of kinetic energy, which contributes to the appearance of larger holes. Finally, for the simulations conducted at a velocity of $2.4662\sigma/\tau$, the viscous dissipation energy is insufficient to stabilize the disk, causing it to break apart or fragment.

Moreover, to provide further insights corresponding to lower-velocity conditions, Fig. S1 and S2 in the ESI† present figures similar to Fig. 5, which show the disk thickness profiles for collisions at a velocity of $V = 1.5690\sigma/\tau$ for pure water and surfactant-laden droplets (above the CAC), respectively, at comparable time instances. These lower-velocity cases correspond to conditions where no hole emergence is observed. It is evident that for pure water, the collision energy dissipates more rapidly, leading to a thinner and less stable disk. In contrast, the presence of surfactants results in a more uniform and stable disk structure. However, at higher velocities, the emergence of holes leads to a less uniform disk, even in the case of surfactant-laden droplets (Fig. 5e–g). To illustrate this clearer, we have provided a movie as the ESI† (see the ESI†), which shows the head-on collision of water droplets (top panel) and surfactant-laden droplets above the CAC (bottom panel) at a velocity of $V = 2.2415\sigma/\tau$. Two different views are presented: a side and a disk view (along the x-axis) to illustrate the evolution of the disk. The movie clearly highlights the significant differences in disk dynamics between pure water and surfactant-laden droplets. The most notable difference is that in the case of pure water, following the collision, the droplets deform into flattened disks that expand to their maximum diameter. Thereafter, the disk contracts, and the system undergoes damped oscillations ('beating') until the kinetic energy is dissipated. However, such oscillations and beating are absent in the case of

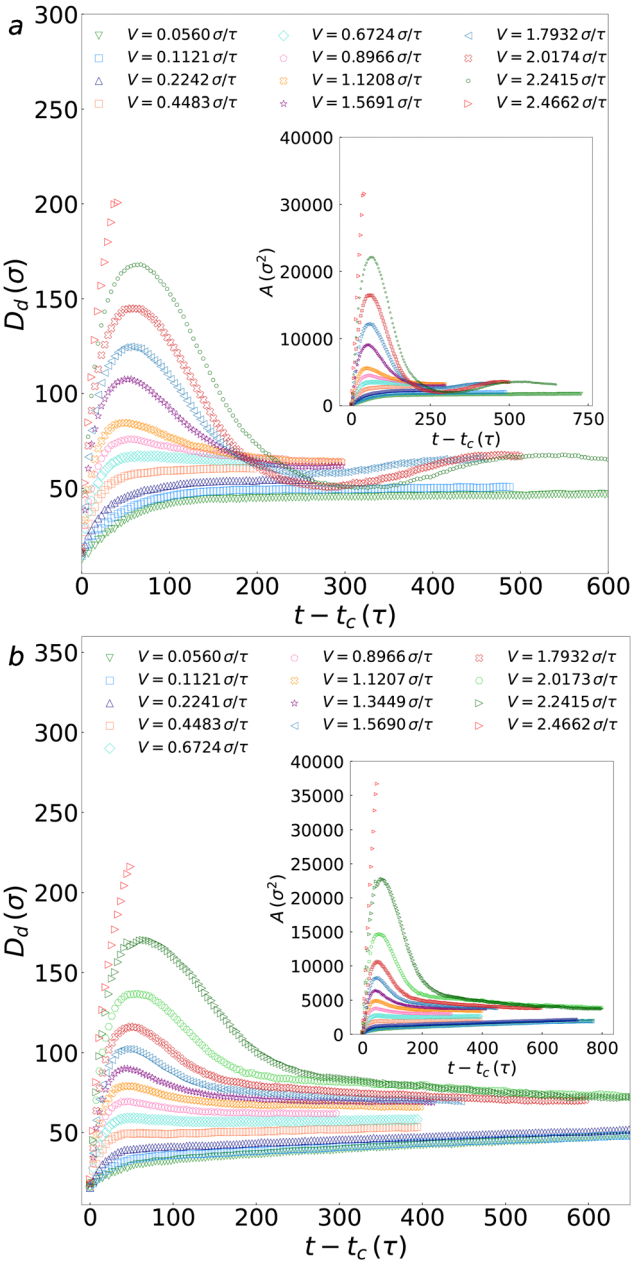

Fig. 5 Disk dynamics during head-on collisions of (a) water droplets and (b) surfactant-laden droplets (above CAC) at different velocities. The area of the disk is shown in the inset of the figure.

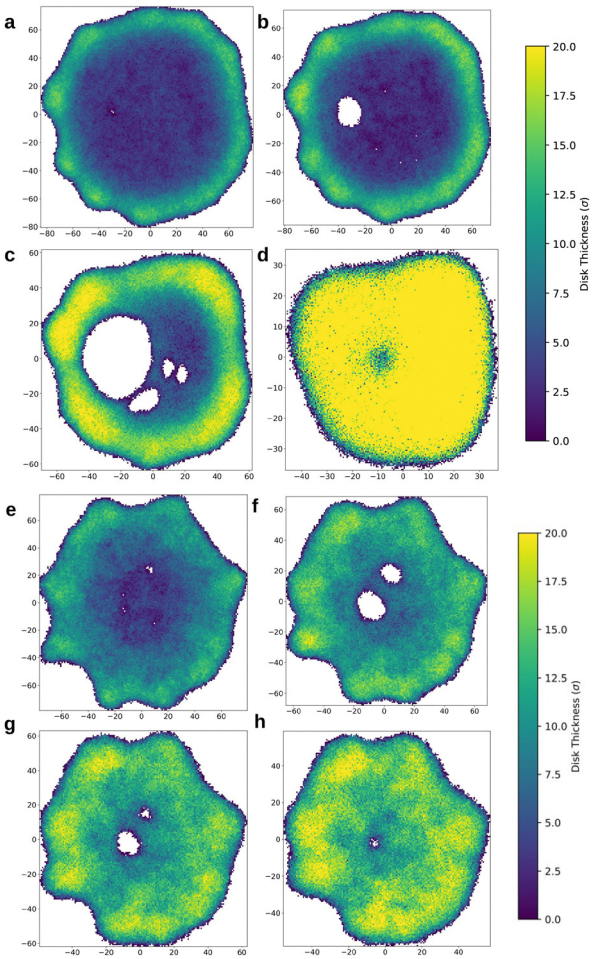

Fig. 6 The plots show a comparison of disks for (a)–(d) pure water and (e)–(h) surfactant-laden droplets above the CAC. The plot illustrates the thickness of the disk, showing that in the case of pure water, there is a stronger flow towards the rim of the disk, which leads to a thinner middle region and larger holes. In contrast, for surfactant-laden droplets, there is a weaker flow, resulting in a thicker middle region and smaller holes. The view of the disk is oriented along the x axis. For pure water, the time sequences are as follows: (a) $t \simeq 90.75\tau$, (b) $t \simeq 104\tau$, (c) $t \simeq 130\tau$, and (d) $t \simeq 192\tau$. For cases above the CAC, the time sequences are: (e) $t \simeq 108.75\tau$, (f) $t \simeq 143.5\tau$, (g) $t \simeq 161.0\tau$, and (h) $t \simeq 175.25\tau$. In our simulations, hole emergence for pure water occurs at approximately $t \simeq 91\tau$. For surfactant-laden droplets, holes (cavities) emerged at approximately $t \simeq 100\tau$ below the CAC (not shown) and $t \simeq 109\tau$ above the CAC.

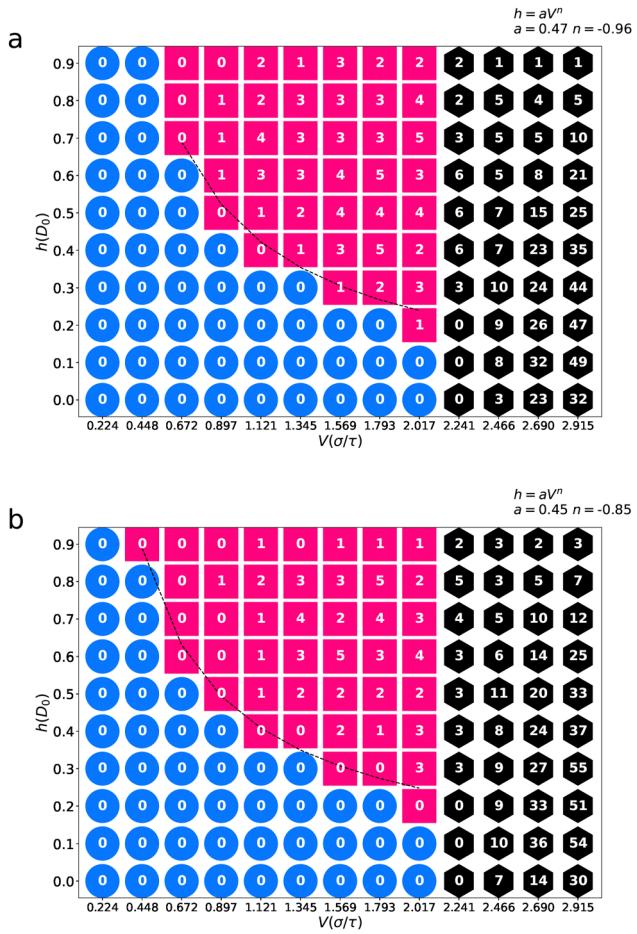

Fig. 7 State diagrams illustrating the outcomes of (a) water droplet and (b) surfactant-laden (above CAC) droplet collisions. The diagrams show the regions corresponding to different collision outcomes: coalescence (blue circles), separation (red squares), and splattering (black hexagons). The data have been mapped as a function of collision parameters: velocity and offset. The boundary between coalescence and separation, estimated with a power law fit with parameters given in the top right corner, is indicated by a dotted black line. Each symbol in the diagram is labelled with a number representing the number of satellite droplets produced.

surfactant-laden droplets, which is attributed to enhanced energy dissipation.

3.2 Off-centre collision

Moving further, in this section, we analyse off-centre collisions where two droplets collide with an offset distance (h in Fig. 1f) between their centres of mass. These collisions are similar to head-on collisions, except that they involve rotational motion of the merged mass. According to our simulations, three different scenarios may occur: coalescence, separation, and splattering. Separation leads to stretching (Fig. 1g) and can result in the formation of satellite droplets (Fig. 1h). Splattering occurs when the velocity is high and the viscous dissipation energy cannot fully absorb the kinetic energy. As a result, the system falls apart, producing many satellite droplets (Fig. 1i).

Fig. 7a and b present collision outcomes for water and surfactant-laden droplets, respectively, in the form of state diagrams. Higher velocities and larger offsets lead to a higher probability of separation. In each case, the number inside the symbol indicates the number of satellite droplets produced during separation. The boundary between coalescence and separation is estimated as a black dashed line. At low velocities, coalescence is the dominant outcome. For low velocities $V \lesssim 0.8\sigma/\tau$ and large offsets $h/D_0 \gtrsim 0.5$, careful comparison of the two phase diagrams shows that the water droplets have a greater tendency to coalesce, due to the higher surface tension in comparison with surfactant-laden droplets. Moreover, the tendency for coalescence weakens at higher velocities. When the offset is large and the droplets just touch each other's surfaces, surface tension becomes more important and can

determine the fate of the collision. However, at lower offsets, viscosity plays a larger role in determining the outcome as it can dissipate more kinetic energy.

Regarding the number of satellite droplets, water collisions generally produce more satellite droplets, which is presumably again due to the lower viscosity. In both cases, in runs with velocities above $V = 2.2415\sigma/\tau$, it is found that splattering occurs, and generally more fragments are produced again in the case of water droplets. To be more precise, for the case of $V = 2.2415\sigma/\tau$, with a small offset ($h < 0.3$), the process can still be considered coalescence. Although several very tiny satellite droplets are formed, they are not counted as satellites due to their extremely small size, and the two droplets merge, as shown in the movie in the ESI.†

4 Conclusions

In this study, we analyzed various properties during the collision of water droplets and surfactant-laden droplets, revealing the collision dynamics through energy balance, bridge growth rate, and satellite droplet counts to quantify the high energy collisions and splattering. We observe that in the case of coalescence, the bridge grows according to a power-law regime, while in the case of collision, an initial linear regime emerges, followed by a power-law regime. This linear regime grows and becomes more dominant by increasing the collision velocity, and above a certain velocity ($V \simeq 0.23\sigma/\tau$ for water and $V \simeq 0.45\sigma/\tau$ for surfactant-laden droplets in our study), the power-law growth is not present and the bridge growth is linear from the outset. We further analysed the later time disk dynamics, which appears to be dominated in surfactant-laden droplets by the effect of viscosity. The lower viscous dissipation energy in the case of water correlates with the creation of a larger disk and the appearance of larger holes. The lower energy dissipation in the case of water droplets is also to be held responsible for the oscillation of the disk dimensions in time, a phenomenon not observed in surfactant-laden droplets. As a major component of the study, we quantified offset collisions for both cases, and a detailed phase diagram was created to compare the different possible outcomes: coalescence, separation, and splattering, and in particular to locate the parameters at which the behaviour undergoes a change. At small offsets, coalescence transitions immediately to splattering above a threshold velocity. Moreover, the onset of splattering appears to be independent of offset and happens even with head-on collisions. At the highest offsets $h \gtrsim 0.7D_0$, the number of satellite droplets arising from splattering drops suddenly (presumably the majority of the droplet fluid passes by without significant interaction). Satellite droplets are also much rarer in the separation regime when offset is large and velocity fairly slow. In addition, it was observed that the number of satellite droplets is higher in the case of water droplet collisions. Finally, we discussed the regimes of cavity formations in the disk-like structures and elucidated their characteristics, such as their thickness. The findings reported here provide overall a broadened understanding of the conditions that lead to different collision outcomes for both water and surfactant-laden droplets.

Conflicts of interest

There are no conflicts to declare.

Data availability

Data for this article are available at repod.icm at **https://repod.icm.edu.pl/dataset.xhtml?persistentId=doi:10.18150/INURJJ**. Any additional data supporting the findings of this study are available from the corresponding author upon reasonable request and can also be provided to referees if needed.

Acknowledgements

This research has been supported by the National Science Centre, Poland, under grant no. 2019/34/E/ST3/00232. We gratefully acknowledge the Polish high-performance computing infrastructure PLGrid (HPC Centers: ACK Cyfronet AGH) for providing computer facilities and support under computational grant no. PLG/2024/017543.

References

1 G. Falkovich, A. Fouxon and M. Stepanov, *Nature*, 2002, **419**, 151–154.
2 in *Combustion of Liquid Fuel Sprays*, ed. A. Williams, Butterworth-Heinemann, Portland, 1990.
3 K. Krishnan and E. Loth, *Int. J. Multiph. Flow*, 2015, **77**, 171–186.
4 Y. Yoon, F. Baldessari, H. D. Ceniceros and L. G. Leal, *Phys. Fluids*, 2007, **19**, 102102.
5 M. I. Khodabocus, M. Sellier and V. Nock, *Adv. Math. Phys.*, 2018, **2018**, 4906016.
6 S. Perumanath, M. K. Borg, M. V. Chubynsky, J. E. Sprittles and J. M. Reese, *Phys. Rev. Lett.*, 2019, **122**, 104501.
7 J. Eggers, J. R. Lister and H. A. Stone, *J. Fluid Mech.*, 1999, **401**, 293–310.
8 D. G. Aarts, H. N. Lekkerkerker, H. Guo, G. H. Wegdam and D. Bonn, *Phys. Rev. Lett.*, 2005, **95**, 164503.
9 J. Sprittles and Y. Shikhmurzaev, *Phys. Fluids*, 2012, **24**, 122105.
10 M. Dudek, D. Fernandes, E. Helno Herø and G. Øye, *Colloids Surf., A*, 2020, **586**, 124265.
11 M. M. Rahman, W. Lee, A. Iyer and S. J. Williams, *Phys. Fluids*, 2019, **31**, 012104.
12 J. D. Berry and R. R. Dagastine, *J. Colloid Interface Sci.*, 2017, **487**, 513–522.
13 P. M. Somwanshi, K. Muralidhar and S. Khandekar, *Phys. Fluids*, 2018, **30**, 092103.
14 P. K. Kirar, K. Alvarenga, P. Kolhe, G. Biswas and K. Chandra Sahu, *Phys. Fluids*, 2020, **32**, 052103.

15 S. Bayani, Y. Tabe, Y. T. Kang, S. H. Lee and C. K. Choi, *J. Flow Visualization Image Process.*, 2018, **25**, 191–205.
16 M. Brik, S. Harmand and I. Zaaroura, *Colloids Surf., A*, 2021, **629**, 127429.
17 C. R. Anthony, M. T. Harris and O. A. Basaran, *Phys. Rev. Fluids*, 2020, **5**, 033608.
18 V. R. Kern, T. Sæter and A. Carlson, *Phys. Rev. Fluids*, 2022, **7**, L081601.
19 M. Heinen, M. Hoffmann, F. Diewald, S. Seckler, K. Langenbach and J. Vrabec, *Phys. Fluids*, 2022, **34**, 042006.
20 M. Geri, B. Keshavarz, G. H. McKinley and J. W. M. Bush, *J. Fluid Mech.*, 2017, **833**, R3.
21 M. Abouelsoud and B. Bai, *Phys. Fluids*, 2021, **33**, 063309.
22 P. J. Dekker, M. A. Hack, W. Tewes, C. Datt, A. Bouillant and J. H. Snoeijer, *Phys. Rev. Lett.*, 2022, **128**, 028004.
23 E. Calvo, E. de Malmazet, F. Risso and O. Masbernat, *Ind. Eng. Chem. Res.*, 2019, **58**, 15573–15587.
24 V. S. Sivasankar, D. R. Hines and S. Das, *Langmuir*, 2022, **38**, 14084–14096.
25 M. R. Otazo, R. Ward, G. Gillies, R. S. Osborne, M. Golding and M. A. K. Williams, *Soft Matter*, 2019, **15**, 6383–6391.
26 C. Vannozzi, *Phys. Fluids*, 2019, **31**, 082112.
27 S. Arbabi and P. E. Theodorakis, *Macromol. Theory Simul.*, 2023, **32**, 2300017.
28 O. Massarweh and A. S. Abushaikha, *Energy Rep.*, 2020, **6**, 3150–3178.
29 M. Denys, P. Deuar, Z. Che and P. E. Theodorakis, *Phys. Fluids*, 2022, **34**, 095126.
30 S. Arbabi, P. Deuar, M. Denys, R. Bennacer, Z. Che and P. E. Theodorakis, *Soft Matter*, 2023, **19**, 8070–8080.
31 S. Arbabi, P. Deuar, M. Denys, R. Bennacer, Z. Che and P. E. Theodorakis, *Phys. Fluids*, 2023, **35**, 063329.
32 S. Arbabi, P. Deuar, R. Bennacer, Z. Che and P. E. Theodorakis, *Phys. Fluids*, 2024, **36**, 023340.
33 Y. R. Zhang and K. H. Luo, *Langmuir*, 2019, **35**, 8896–8902.
34 W. Liu, N. Li, Z. Sun, Z. Wang and Z. Wang, *Langmuir*, 2021, **38**, 411–421.
35 B. Wyatt, *Comput. Math. Appl.*, 1994, **28**, 175–208.
36 M. Svanberg, L. Ming, N. Marković and J. B. Pettersson, *J. Chem. Phys.*, 1998, **108**, 5888–5897.
37 S. Murad and C. K. Law, *Mol. Phys.*, 1999, **96**, 81–85.
38 I.-B. Chun, M. Y. Ha, J. Jang and H. S. Yoon, *Bull. Korean Chem. Soc.*, 2011, **32**, 2027–2031.
39 L. Tugend, S. Homes and J. Vrabec, *Langmuir*, 2025, **41**, 1480–1490.
40 D. Greenspan, *Comput. Math. Appl.*, 1990, **19**, 91–97.
41 Y. R. Zhang, X. Z. Jiang and K. H. Luo, *J. Comput. Sci.*, 2016, **17**, 457–462.
42 X. Z. Jiang, Y. R. Zhang and K. H. Luo, *J. Nanosci. Nanotechnol.*, 2016, **16**, 8380–8386.
43 Y. R. Zhang, Z. Zhao, K. H. Luo and B. Shi, *J. Mol. Liq.*, 2021, **341**, 117383.
44 W. Liu, N. Li, Z. Sun, Z. Wang and Z. Wang, *J. Mol. Liq.*, 2022, **354**, 118841.
45 Y.-F. Wang, Y.-B. Wang, Z.-H. Cai, Q. Ma, Y.-R. Yang, S.-F. Zheng, D.-J. Lee and X.-D. Wang, *J. Fluid Mech.*, 2024, **979**, A25.
46 M. L. Nietiadi and H. M. Urbassek, *Sci. Rep.*, 2022, **12**, 10699.
47 J. Qian and C. K. Law, *J. Fluid Mech.*, 1997, **331**, 59–80.
48 K.-L. Pan, Y.-H. Tseng, J.-C. Chen, K.-L. Huang, C.-H. Wang and M.-C. Lai, *J. Fluid Mech.*, 2016, **799**, 603–636.
49 K.-L. Huang, K.-L. Pan and C. Josserand, *Phys. Rev. Lett.*, 2019, **123**, 234502.
50 A. Munnannur and R. D. Reitz, *Int. J. Multiph. Flow*, 2007, **33**, 873–896.
51 K.-L. Pan, P.-C. Chou and Y.-J. Tseng, *Phys. Rev. E: Stat., Nonlinear, Soft Matter Phys.*, 2009, **80**, 036301.
52 L. H. Carnevale, P. Deuar, Z. Che and P. E. Theodorakis, *Phys. Fluids*, 2023, **35**, 074108.
53 L. H. Carnevale, P. Deuar, Z. Che and P. E. Theodorakis, *Phys. Fluids*, 2024, **36**, 033301.
54 Y. Wu, F. Wang, S. Zheng and B. Nestler, *Soft Matter*, 2024, **20**, 1523–1542.
55 J. D. Paulsen, R. Carmigniani, A. Kannan, J. C. Burton and S. R. Nagel, *Nat. Commun.*, 2014, **5**, 3182.
56 J. D. Paulsen, *Phys. Rev. E: Stat., Nonlinear, Soft Matter Phys.*, 2013, **88**, 063010.
57 M. Gross, I. Steinbach, D. Raabe and F. Varnik, *Phys. Fluids*, 2013, **25**, 052101.
58 L. Duchemin, J. Eggers and C. Josserand, *J. Fluid Mech.*, 2003, **487**, 167–178.
59 S. Thoroddsen, K. Takehara and T. Etoh, *J. Fluid Mech.*, 2005, **527**, 85–114.
60 J. D. Paulsen, J. C. Burton, S. R. Nagel, S. Appathurai, M. T. Harris and O. A. Basaran, *Proc. Natl. Acad. Sci. U. S. A.*, 2012, **109**, 6857–6861.
61 J. Eggers, J. E. Sprittles and J. H. Snoeijer, *Annu. Rev. Fluid Mech.*, 2024, **57**, 61–87.
62 W. G. Chapman, K. E. Gubbins, G. Jackson and M. Radosz, *Fluid Phase Equilib.*, 1989, **52**, 31–38.
63 E. A. Müller and K. E. Gubbins, *Ind. Eng. Chem. Res.*, 2001, **40**, 2193–2211.
64 C. Avendaño, T. Lafitte, A. Galindo, C. S. Adjiman, G. Jackson and E. A. Müller, *J. Phys. Chem. B*, 2011, **115**, 11154–11169.
65 C. Avendaño, T. Lafitte, A. Galindo, C. S. Adjiman, E. A. Müller and G. Jackson, *J. Phys. Chem. B*, 2013, **117**, 2717–2733.
66 D. Sergi, G. Scocchi and A. Ortona, *J. Chem. Phys.*, 2012, **137**, 094904.
67 E. A. Müller and G. Jackson, *Annu. Rev. Chem. Biomol. Eng.*, 2014, **5**, 405–427.
68 T. Lafitte, A. Apostolakou, C. Avendaño, A. Galindo, C. S. Adjiman, E. A. Müller and G. Jackson, *J. Chem. Phys.*, 2013, **139**, 154504.
69 P. E. Theodorakis, E. A. Müller, R. V. Craster and O. K. Matar, *Soft Matter*, 2015, **11**, 9254–9261.
70 P. E. Theodorakis, E. R. Smith, R. V. Craster, E. A. Müller and O. K. Matar, *Fluids*, 2019, **4**, 176.
71 O. Lobanova, PhD thesis, Imperial College London, 2014.
72 O. Lobanova, A. Mejia, G. Jackson and E. A. Müller, *J. Chem. Thermodyn.*, 2016, **93**, 320–336.
73 P. Morgado, O. Lobanova, E. A. Müller, G. Jackson, M. Almeida and E. J. Filipe, *Mol. Phys.*, 2016, **114**, 2597–2614.

74 P. E. Theodorakis, E. A. Müller, R. V. Craster and O. K. Matar, *Langmuir*, 2015, **31**, 2304–2309.
75 P. E. Theodorakis, E. A. Müller, R. V. Craster and O. K. Matar, *Curr. Opin. Colloid Interface Sci.*, 2014, **19**, 283–289.
76 P. E. Theodorakis, E. R. Smith and E. A. Müller, *Colloids Surf., A*, 2019, **581**, 123810.
77 A. P. Thompson, H. M. Aktulga, R. Berger, D. S. Bolintineanu, W. M. Brown, P. S. Crozier, P. J. in 't Veld, A. Kohlmeyer, S. G. Moore, T. D. Nguyen, R. Shan, M. J. Stevens, J. Tranchida, C. Trott and S. J. Plimpton, *Comput. Phys. Commun.*, 2022, **271**, 108171.
78 B.-X. Li, X.-H. Li and M. Chen, *Phys. Fluids*, 2017, **29**, 012003.